Magnon Straintronics: Reconfigurable Spin-Wave Routing in Strain-Controlled Bilateral Magnetic Stripes

A. V. Sadovnikov
Laboratory "Metamaterials," Saratov State University, Saratov 410012, Russia
and Kotel'nikov Institute of Radioengineering and Electronics, RAS, Moscow 125009, Russia

A. A. Grachev, S. E. Sheshukova, Yu. P. Sharaevskii, A. A. Serdobintsev, and D. M. Mitin
Laboratory "Metamaterials," Saratov State University, Saratov 410012, Russia

S. A. Nikitov
Laboratory "Metamaterials," Saratov State University, Saratov 410012, Russia
and Kotel'nikov Institute of Radioengineering and Electronics, RAS, Moscow 125009, Russia

(Received 6 November 2017; published 21 June 2018)

We observe and explain theoretically strain-induced spin-wave routing in the bilateral composite multilayer. By means of Brillouin light scattering and microwave spectroscopy, we study the spin-wave transport across three adjacent magnonic stripes, which are strain coupled to a piezoelectric layer. The strain may effectively induce voltage-controlled dipolar spin-wave interactions. We experimentally demonstrate the basic features of the voltage-controlled spin-wave switching. We show that the spin-wave characteristics can be tuned with an electrical field due to piezoelectricity and magnetostriction of the piezolayer and layered composite and mechanical coupling between them. Our experimental observations agree with numerical calculations.

DOI: 10.1103/PhysRevLett.120.257203

Advances in the micro- and nanoscale engineering of insulating-based magnetic structures opens a promising alternative to signal processing by spin waves in beyond-CMOS computing technology, based on magnonic networks [1–5] with low-level energy consumption. The micro- and nanosized magnetic structures emerge as a promising basis for magnonic integrated circuits [1,6–10], which overcomes the inherent limits of the conventional CMOS-based electronics [11–13]. The quasiparticles associated with the eigenexcitations of magnetic materials known as spin waves (SWs) or magnons can be used as information carriers in the magnonic circuits; however, the magnetic field tunability of magnonic devices is inherently slow and needs significant power consumption. In contrast, the electrical tuning is potentially much faster and more relevant to energy-consumption-based applications [14–17]. The ability to control spin-wave transport by both the electric and magnetic field will enable the development of smaller and more efficient magnonic devices.

Recent theoretical and experimental studies suggest that strain can be used to engineer energy-efficient complicated 2D and 3D piezoelectric material and heterostructures based, e.g., on semiconductors [18], ferroelectrics [19], polar metals [20], piezoelectric crystals or ceramics [21], graphene layers [22–24], and nanowire arrays [25]. It was also shown that it is possible to induce a ferromagnetic resonance frequency shift due to the effect of the electric-field-to-magnetic-field conversion [26,27]. The effect of the electric field on the magnetic configuration results from the modification of the effective internal magnetic field. The latter is changed due to inverse magnetostriction (Villary effect) as a result of the local deformation of the magnetic film.

It was demonstrated experimentally that the spin-wave coupling can be effectively used to manipulate magnon transport [28], where it underlies the operational regimes of versatile components of magnonic networks: the dual channel directional coupler [28,29], spin-wave power splitter [4,30], and tunable frequency-selective all-magnonic unit [2,31]. This demonstration of propagating spin-wave coupling opens the door to both the study of nonlinear spin-wave dynamics [32] and mechanisms of spin-wave coupling manipulation.

The combination of strain tuning and spin-wave coupling can underlie a new branch of functional magnonics—magnon straintronics. Thus, the voltage-driven spin-wave operation can be potentially used for low-dissipation spin-wave-based logic circuits [33] and memory elements [34].

In this Letter, we report the direct measurement of voltage-controlled spin-wave switching in a bilateral composite structure, where the dipolar stray fields produced by the spin wave in one magnetic stripe affects the spin-wave behavior in two neighbor stripes. By utilizing Brillouin light scattering (BLS) spectroscopy, we demonstrate the dynamic

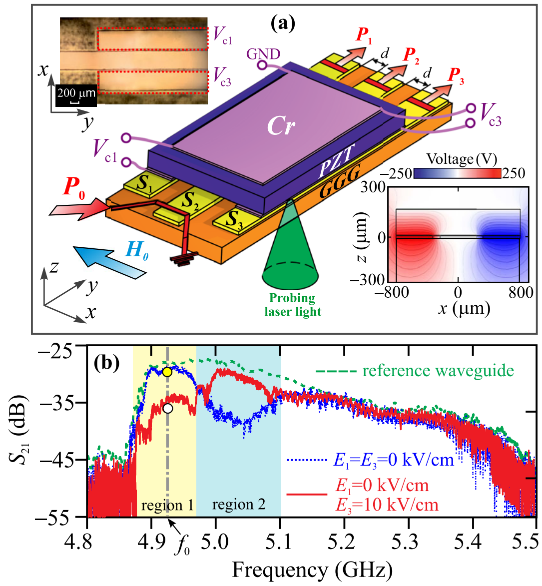

FIG. 1. (a) Schematic view of bilateral magnonic stripes. Top inset: Microphotograph of the fabricated YIG stripes. Red dotted rectangles denote the electrodes. Bottom inset: The distribution of the voltage in the case of $V_{c1} = 250$ V and $V_{c3} = -250$ V. (b) The spin-wave transmission through stripe S_2 when voltage is not applied (blue dashed curve) and in the case of applied voltage (red solid curve).

strain-mediated coupling of spin waves. We show that the spin-wave characteristics can be tuned effectively with an electrical field due to piezoelectricity and magnetostriction of the piezolayer and layered composite and mechanical coupling between them, which enables effective spin-wave routing in parallel magnonic networks.

Our device is three adjacent magnonic stripes, which form three spin-wave channels as shown schematically in Fig. 1(a). The structure consists of three $t = 10$-μm-thick yttrium iron garnet [35] [$Y_3Fe_5O_{12}$ (111), YIG] stripes of $w = 500$ μm width placed on a 500-μm-thick gadolinium gallium garnet [$Gd_3Ga_5O_{12}$ (111), GGG] substrate. The saturation magnetization of YIG is $M_0 = 139$ G. Side-coupled stripes have an edge-to-edge spacing of $d = 40$ μm. Hereafter, we will call these stripes S_1, S_2, and S_3 as denoted in Fig. 1(a). The length along the long side of the waveguides was 4 mm for S_1 and S_3 and 10 mm for S_2. Spin-wave excitation was realized by the 1-μm-thick input microstrip antenna of 30 μm width. An output antenna with the same dimensions was placed only at stripe S_2 at the distance of 5.5 mm from the input microstrip. The bias magnetic field $H_0 = 1100$ Oe was applied along the x axis. A 500-nm-thick chrome (Cr) electrode was deposited on the top surfaces of a $1580 \times 4000 \times 200$ μm^3 piezoelectric ceramic layer from lead zirconate titanate (PZT) [36]. Because of the sufficiently thick PZT layer, the upper electrode has no effect on spin-wave propagation in YIG. In order to neglect the influence of the metal layer on the spin-wave dynamics, two 50-nm-thick Cr electrodes were deposited on the other side of the PZT [37–40]. Strain coupling of the PZT and YIG stripes [26] was achieved in the experiment using the heat-cured two-part epoxy strain gage adhesive [41].

The electric voltage $V_{c1,3}$ in the range of $-250\ldots250$ V is applied to the electrodes in order to induce the strain both in the PZT layer and on the surface of YIG due to the strain coupling. The distribution of electric voltage is shown in the bottom inset in Fig. 1(a) for the case of $V_{c1} = 250$ V and $V_{c3} = -250$ V. Next, by means of microwave spectroscopy (vector network analyzer), we measure the absolute value of the S_{21} coefficient which corresponds to the spin-wave transmission through stripe S_2. The noticeable dip in the frequency range $4.975 < f < 5.1$ GHz at the transmission response [blue dashed curve and region 2 in Fig. 1(b)], when $E_1 = E_3 = 0$ kV/cm, corresponds to the regime when input power P_0 is transmitted from stripe S_2 to stripes S_1 and S_3. When we apply the voltage to one of the electrodes ($E_1 = 0$ kV/cm and $E_3 = 10$ kV/cm), a peak in the same frequency range (region 2) is clearly observed in the transmission response [red solid curve in Fig. 1(b)]. This peak corresponds to the full power transmittance through stripe S_2. We provide also the spin-wave transmission characteristic of the reference YIG stripe of 500 μm width [green dashed curve in Fig. 1(b)], which is typical for the Daemon-Eshbach configuration [42,43] demonstrating the monotonic decrease of S_{21} with the increase of frequency. Thus, the microwave spectroscopy shows that the voltage-controlled tunability of spin-wave transmission is possible. The nature of this dip and peak will be revealed further from numerical simulations and BLS experiments.

We use the finite-element simulation software based on COMSOL Multiphysics [44–47] and MATLAB [48] with the micromagnetic simulations [49] to solve the self-consistent 3D problem. First, we find the strain, mediated in each of the YIG stripes by the voltage applied to the PZT layer. Second, we compute the internal magnetic field profile in adjacent magnetic stripes. Next, we use the calculated internal magnetic field profile in the micromagnetic simulations, and we use the finite-element method [28,46,50] to calculate the eigenmode spectra and mode profiles of the laterally parallel magnetic stripes with the nonuniform magnetization configurations.

We start from solving the linear magnetostrictive problem [51]. Figures 2(a) and 2(b) demonstrate [52] the lateral and axial deformation of the PZT layer and distribution of stress tensor component S_{xx} in the case of $V_{c1} = 250$ V and $V_{c3} = -250$ V. Thus, the electrical field E causes an interface strain in YIG due to the piezoelectric effect. Next, the inverse magnetostrictive effect produces the local transformation of the internal magnetic field H_{int} profile. Since SWs are propagated along three waveguiding channels, which are formed as a result of the shape anisotropy of magnetic structures, the variation of H_{int} affects the spin-wave characteristic. In particular, if the positive or negative

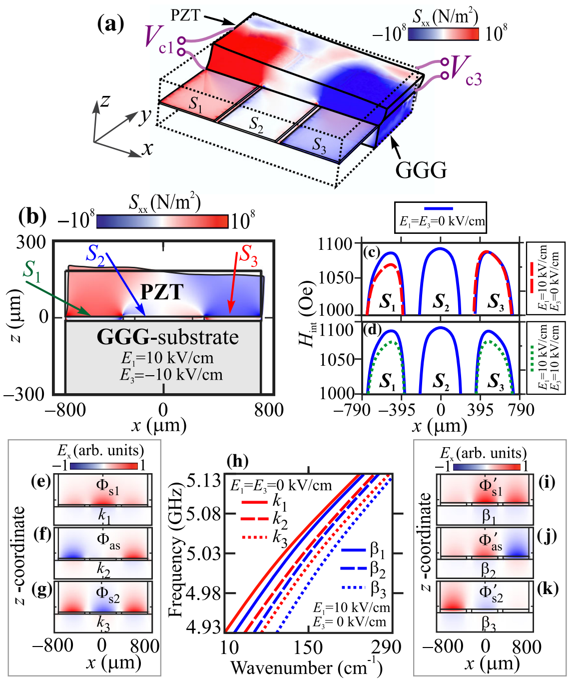

FIG. 2. (a), (b) The distribution of stress tensor component S_{xx} showing a local deformation of the PZT layer and induced stress on the surface of YIG stripes. (c), (d) The voltage-induced transformation of the internal magnetic field profile. (e)–(g) Eigenmodes of the adjacent magnetic stripes in the case of $E_1 = E_3 = 0$ kV/cm. (h) The dispersion of the two symmetric and one antisymmetric modes, when $E_1 = E_3 = 0$ kV/cm (red curves) and $E_1 = 10$ kV/cm and $E_3 = 0$ kV/cm (blue curves). (i)–(k) Eigenmodes of the adjacent magnetic stripes in the case of $E_1 = E_3 = 10$ kV/cm.

value of the electric field is applied to the electrodes on the PZT layer, the value of H_{int} is reduced or increased, respectively.

For a more precise understanding of our observations, we focus on the spin-wave spectra in the bilateral stripes. The dipolar coupling of the propagating SW in isolated stripes leads to the splitting of the spin-wave dispersion [28,53–55] into three SW modes with wave numbers k_1, k_2, and k_3 [see Fig. 2(h)]. Thus, the eigenmode spectrum of the identical three adjacent stripes consists of the orthogonal system [28,56] of antisymmetric Φ_{as} and two symmetric (Φ_{s1}, Φ_{s2}) modes [see Figs. 2(e)–2(g)] with the wave numbers of k_2, k_1, and k_3, respectively.

The appropriate values of the piezoelectric voltage coefficients [36] provide sufficient strain to change the internal magnetic field in stripe S_1 or/and S_3, as shown in Figs. 2(c) and 2(d). This leads to the transformation of eigenmode profiles and dispersion characteristics. Thus, if $E_1 = 10$ kV/cm and $E_3 = 0$ kV/cm, the dispersion of the quasisymmetric Φ'_{s1}, Φ'_{s2} modes [Figs. 2(i) and 2(k)] and quasiantisymmetric eigenmode Φ'_{as} [Fig. 2(j)] is shown in Fig. 2(h) with blue curves. The wave numbers β_1, β_3, and β_2 correspond to these modes.

To demonstrate the switching in spin-wave propagation along the bilateral stripes, we use the BLS technique in the backscattering configuration [57–59]. Probing laser light with a 532 nm wavelength was focused on the transparent GGG side of the composite structure [as shown in Fig. 1(a)]. Figures 3(a)–3(d) show the pseudocolor-coded two-dimensional 4×1.6 mm^2 spatial maps of the recorded BLS intensity $I(x, y)$ at the frequency of $f_1 = 4.925$ GHz and level of input power of $P_0 = -15$ dBm. To complement and further understand the experimental data, micromagnetic simulations [49,60] were performed to yield the phase of the propagating spin wave [Figs. 3(e)–3(h)]. If no electric field is applied to the sample, the coupling length for three-channel directional coupler $L_0 = \pi/|k_3 - k_1|$ is defined as the distance at which the spin-wave energy is transmitted from S_2 to both S_1 and S_3 [see Figs. 3(a) and 3(e)]. We emphasize that the eigenmodes ($\Phi_{s1,2,\mathrm{as}}$) beat along the direction of propagation leads to the formation of the periodic pattern of spin-wave intensity [28,53,61,62]. The calculation results agree qualitatively with the BLS data, and it should be noted that the three magnetic stripes provide a smaller value of the spin-wave coupling length in comparison with the two-channel configuration. This is important due to the finite spin-wave propagation length. If the voltage is applied to one or both electrodes, the spatial spin-wave intensity distribution is transformed. If $E_1 = 0$ kV/cm and $E_3 = 10$ kV/cm, the spin-wave power exchange is observed between stripes S_1 and S_2 [Figs. 3(b) and 3(f)]. In this case, the coupling length can be estimated as $L_3 = \pi/\Delta\beta$, where $\Delta\beta = |\beta_2 - \beta_1|$. This agrees well with the data obtained from the microwave measurement [Fig. 1(b)]. The splitting of the input power between S_2 and S_3 occurs if $E_1 = 10$ kV/cm and $E_3 = 0$ kV/cm [Figs. 3(c) and 3(g)]. It is worth noting that $L_0 < L_{1,3}$ from the BLS experiment, micromagnetic simulations, and data from the dispersion calculation. If the voltage is applied to both electrodes ($E_1 = E_3 = 10$ kV/cm), the spin-wave coupling is not efficient between S_2, S_1, and S_3 due to the synchronous increase of the value of ΔH_1 and ΔH_3 as shown in Fig. 2(d). In this case, the SW propagates along S_2 [see Figs. 3(d) and 3(h)]. Specifically designed geometry offers the possibility to tune the coupling characteristics. In particular, the variation of the width of each YIG stripes in the range $100 < w < 1000$ μm leads to the coupling length increase by a factor of 5 [Fig. 3(i)]. At the same time, the difference of the internal magnetic field between the positions of center of the ith and stripe S_2 reads as $\Delta H_i(x = x_i)$ (where $i = 1, 3$) and also varied from 14 to 2 Oe as shown in Fig. 3(i). Thus, the optimal width of the YIG stripes should provide the optimal value of ΔH to tune the value of the coupling length to be comparable with the spin-wave propagation length.

Next, to validate our findings on the spin-wave switching mechanism, we measure the frequency dependence of the BLS signal integrated over each stripe at the position of $y = 2L_0 = 3.0$ mm. It is clearly seen from Fig. 3(j) that there is a distinguished dip in the frequency range

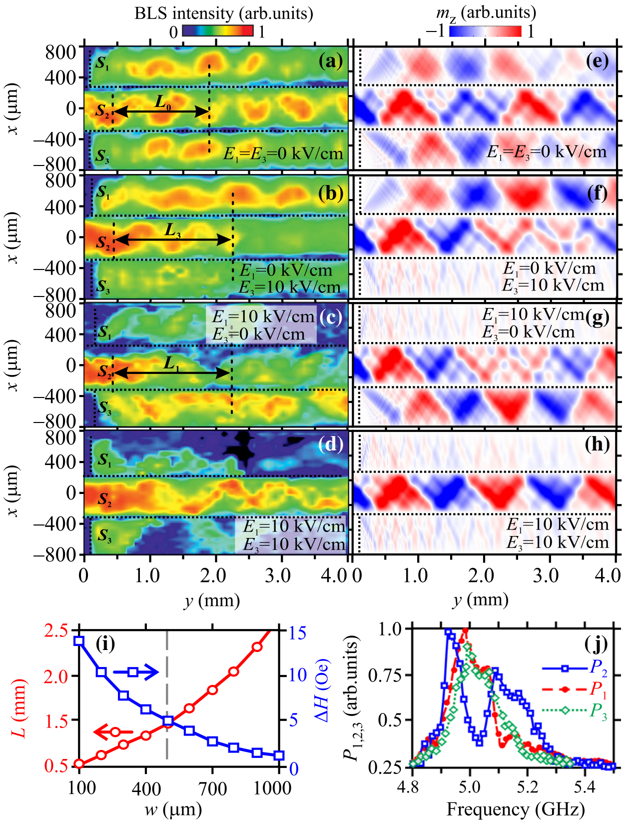

FIG. 3. (a)–(d) The BLS spin-wave intensity at the frequency of $f_1 = 4.925$ GHz at the different values of the applied voltages (denoted in the figure); (c)–(h) snapshots of the dynamic out-of-plane component of dynamic magnetization calculated by means of micromagnetic simulations at the excitation frequency of $f_1 = 4.925$ GHz. Edges of stripes are guided with dotted lines. (i) Calculated coupling length and difference of the internal magnetic field as a function of the stripe width. The curve is a guide for the eyes. (j) Frequency dependence of the output signal P_1, P_2, and P_3 in stripe S_1, S_2, and S_3, respectively. All the shown data were obtained at $H_0 = 1100$ Oe.

of $4.95 < f < 5.1$ GHz in the signal obtained at S_2 [compare with Fig. 1(b)]. The peaks in the same frequency range in the signals from S_1 and S_3 are also observed. To show the transformation of the spin-wave intensity distribution between the stripes, we demonstrate the frequency dependence of BLS signal $P_{1,2}$ at the y position of $y = 2L_0 = 3.6$ mm when $E_1 = E_3 = 0$ kV/cm [see Fig. 4(a)] and $E_1 = 10$ kV/cm, $E_3 = 0$ kV/cm [see Fig. 4(b)]. In the frequency region between $f_1 = 4.925$ GHz and $f_2 = 4.985$ GHz, the signal attenuation in S_2 is visible, and this corresponds to the regime when the power is nonequally divided between the magnonic stripes. When $f > 4.985$, the spin-wave power is mainly localized in the central stripe S_2. It should be noted in the case of $E_1 = 10$ kV/cm that only the edge mode [63] is excited in stripe S_1 over the frequency range 4.9–5.1 GHz, as shown in Fig. 4(b). The propagation of the center mode along S_1 is therefore suppressed by the locally adjusted strain.

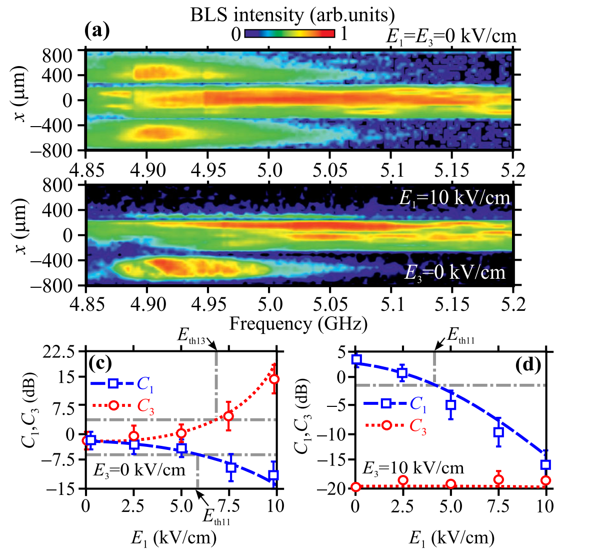

FIG. 4. Frequency dependence of the BLS signal over all three stripes when $E_1 = E_3 = 0$ kV/cm (a) and $E_1 = 10$ kV/cm, $E_3 = 0$ kV/cm. (c) and (d) show the value of the coefficients $C_{1,3}$ (open squares and circles) as a function of E_1 in the case of $E_3 = 0$ kV/cm and $E_3 = 10$ kV/cm, respectively. The dashed dotted lines denote the threshold value of the electric field.

Finally, we study how the power is divided between the spin-wave channels. We introduce the coefficients $C_i = 10\lg(P_i/P_2)$, where $P_i = I_i(x)$ correspond to BLS intensities across the ith stripe. The behavior of $C_{1,3}(E_1)$ is plotted for the case of $E_3 = 0$ kV/cm [see Fig. 4(c)] and $E_3 = 10$ kV/cm [see Fig. 4(d)]. Therefore, we define the threshold electric field $E_{\mathrm{th}ij}$, necessary to switch the output power from the stripe S_j by the variation of the electric field E_i. The necessary value of threshold field is defined at $E = E_{\mathrm{th}}$ when the 5 dB level of the variation of the coefficient C from the value $C(E_1 = 0)$ is reached. In the case of both $E_3 = 0$ kV/cm [Fig. 4(c)] and $E_3 = 10$ kV/cm [Fig. 4(d)], the value of the threshold field is about 5–6 kV/cm. Thus, the proposed strain-reconfigurable three-channel structure demonstrates the efficient voltage-controlled spin-wave switching and can act as a tunable demultiplexer or spin-wave splitter and directional coupler.

In summary, using BLS and microwave spectroscopy we experimentally demonstrated voltage-controlled spin-wave transport along bilateral magnonic stripes. We identified the spin-wave routing between the strain-reconfigurable magnetic channels. A model describing the spin-wave transmission response and predicting its value is proposed. Our work shows that the strain-mediated spin-wave channels provide a useful window into the transformation of the spin-wave spectra and spin-wave dynamics. This revelation is of particular importance when we consider the practical advantages that the composite magnon-straintronic structure could provide to fabricating magnonic platforms for energy-efficient signal processing.

Thus, the three-channel isolator-based directional coupler distinguishes itself as an ideal platform for magnonics in three key aspects: first, dual tunability with both the magnetic and electric field; second, it supports large spin-wave propagation distances, which is appropriate for spin-wave interference in magnonic logic applications; and third, its versatile magnonic component with the voltage-controlled frequency-selective characteristics.

The structure fabrication was supported by RFBR (16-29-14021), BLS measurement was supported by Russian Science Foundation (No.16-19-10283), A. V. S. and S. E. S. acknowledge support of microwave measurements from the Scholarship of the President of Russian Federation (SP-2819.2018.5) and Grant of the President of Russian Federation (MK-3650.2018.9).

[1] A. V. Chumak, V. I. Vasyuchka, A. A. Serga, and B. Hillebrands, Nat. Phys. **11**, 453 (2015).

[2] A. V. Sadovnikov, E. N. Beginin, S. A. Odincov, S. E. Sheshukova, Y. P. Sharaevskii, A. I. Stognij, and S. A. Nikitov, Appl. Phys. Lett. **108**, 172411 (2016).

[3] S. Klingler, P. Pirro, T. Bracher, B. Leven, B. Hillebrands, and A. V. Chumak, Appl. Phys. Lett. **105**, 152410 (2014).

[4] A. V. Sadovnikov, E. N. Beginin, M. A. Morozova, Y. P. Sharaevskii, S. V. Grishin, S. E. Sheshukova, and S. A. Nikitov, Appl. Phys. Lett. **109**, 042407 (2016).

[5] A. Khitun, M. Bao, and K. L. Wang, J. Phys. D **43**, 264005 (2010).

[6] V. V. Kruglyak, S. O. Demokritov, and D. Grundler, J. Phys. D **43**, 264001 (2010).

[7] V. E. Demidov, S. Urazhdin, A. Zholud, A. V. Sadovnikov, A. N. Slavin, and S. O. Demokritov, Sci. Rep. **5**, 8578 (2015).

[8] S. A. Nikitov, D. V. Kalyabin, I. V. Lisenkov, A. N. Slavin, Y. N. Barabanenkov, S. A. Osokin, A. V. Sadovnikov, E. N. Beginin, M. A. Morozova, Y. P. Sharaevsky, Y. A. Filimonov, Y. V. Khivintsev, S. L. Vysotsky, V. K. Sakharov, and E. S. Pavlov, Phys. Usp. **185**, 1099 (2015).

[9] Y. Haiming, O. Kelly, V. Cros, R. Bernard, P. Bortolotti, A. Anane, F. Brandl, F. Heimbach, and D. Grundler, Nat. Commun. **7**, 11255 (2016).

[10] A. V. Sadovnikov, C. S. Davies, V. V. Kruglyak, D. V. Romanenko, S. V. Grishin, E. N. Beginin, Y. P. Sharaevskii, and S. A. Nikitov, Phys. Rev. B **96**, 060401(R) (2017).

[11] ITRS, International Technology Roadmap for Semiconductors (ITRS) 2015 edition, http://www.itrs2.net/itrs-reports.html.

[12] D. Sander, S. O. Valenzuela, D. Makarov, C. H. Marrows, E. E. Fullerton, P. Fischer, J. McCord, P. Vavassori, S. Mangin, P. Pirro, B. Hillebrands, A. D. Kent, T. Jungwirth, O. Gutfleisch, C. G. Kim, and A. Berger, J. Phys. D **50**, 363001 (2017).

[13] S. O. Demokritov, *Spin Wave Confinement: Propagating Waves*, 2nd ed. (Pan Stanford, Singapore, 2017).

[14] N. Lei, T. Devolder, G. Agnus, P. Aubert, L. Daniel, J. Kim, W. Zhao, T. Trypiniotis, R. P. Cowburn, C. Chappert, D. Ravelosona, and P. Lecoeur, Nat. Commun. **4**, 1378 (2013).

[15] E. De Ranieri, P. E. Roy, D. Fang, E. K. Vehsthedt, A. C. Irvine, D. Heiss, A. Casiraghi, R. P. Campion, B. L. Gallagher, T. Jungwirth, and J. Wunderlich, Nat. Mater. **12**, 808 (2013).

[16] M. Buzzi, R. V. Chopdekar, J. L. Hockel, A. Bur, T. Wu, N. Pilet, P. Warnicke, G. P. Carman, L. J. Heyderman, and F. Nolting, Phys. Rev. Lett. **111**, 027204 (2013).

[17] A. Chen and Y. G. Zhao, APL Mater. **4**, 032303 (2016).

[18] A. A. Shevyrin, A. G. Pogosov, A. K. Bakarov, and A. A. Shklyaev, Phys. Rev. Lett. **117**, 017702 (2016).

[19] S. Liu and R. E. Cohen, Phys. Rev. Lett. **119**, 207601 (2017).

[20] D. Varjas, A. G. Grushin, R. Ilan, and J. E. Moore, Phys. Rev. Lett. **117**, 257601 (2016).

[21] H. Jaffe and D. A. Berlincourt, Proc. IEEE **53**, 1372 (1965).

[22] N. Levy, S. A. Burke, K. L. Meaker, M. Panlasigui, A. Zettl, F. Guinea, A. H. C. Neto, and M. F. Crommie, Science **329**, 544 (2010).

[23] T. Fujita, M. B. A. Jalil, and S. G. Tan, Appl. Phys. Lett. **97**, 043508 (2010).

[24] M. T. Ong and E. J. Reed, ACS Nano **6**, 1387 (2012).

[25] Z. L. Wang and J. Song, Science **312**, 242 (2006).

[26] Y. K. Fetisov and G. Srinivasan, Appl. Phys. Lett. **88**, 143503 (2006).

[27] Y. K. Fetisov and G. Srinivasan, Appl. Phys. Lett. **93**, 033508 (2008).

[28] A. V. Sadovnikov, E. N. Beginin, S. E. Sheshukova, D. V. Romanenko, Y. P. Sharaevskii, and S. A. Nikitov, Appl. Phys. Lett. **107**, 202405 (2015).

[29] A. Y. Annenkov and S. V. Gerus, J. Commun. Technol. Electron. **41**, 196 (1996).

[30] A. V. Sadovnikov, A. A. Grachev, E. N. Beginin, S. E. Sheshukova, Y. P. Sharaevskii, and S. A. Nikitov, Phys. Rev. Applied **7**, 014013 (2017).

[31] A. V. Sadovnikov, S. Davies, S. Grishin, V. Kruglyak, D. Romanenko, Y. Sharaevskii, and S. Nikitov, Appl. Phys. Lett. **106**, 192406 (2015).

[32] A. V. Sadovnikov, S. A. Odintsov, E. N. Beginin, S. E. Sheshukova, Y. P. Sharaevskii, and S. A. Nikitov, Phys. Rev. B **96**, 144428 (2017).

[33] A. Khitun, D. E. Nikonov, and K. L. Wang, J. Appl. Phys. **106**, 123909 (2009).

[34] S. Cherepov, P. K. Amiri, J. G. Alzate, K. Wong, M. Lewis, P. Upadhyaya, J. Nath, M. Bao, A. Bur, T. Wu, G. P. Carman, A. Khitun, and K. L. Wang, Appl. Phys. Lett. **104**, 082403 (2014).

[35] CJSC NII "Materialovedenie," Zelinograd, Russia. Magnetostriction constants for YIG: $\lambda_{100} = -1.404 \times 10^{-6}$, $\lambda_{111} = -2.4 \times 10^{-6}$, and saturation magnetostriction $\lambda_s = -2.2 \times 10^{-6}$.

[36] PI Ceramic GmbH, Lederhose, Germany. Density $\rho = 7.8$ g/cm^3, relative permittivity $\varepsilon = 2400$, relative permeability $\mu = 1$, piezoelectric voltage coefficient $d_{31} = -210 \times 10^{-12}$ C/N, and $d_{33} = 500 \times 10^{-12}$ C/N.

[37] The thickness of the Cr electrode was smaller than the skin depth for microwaves over the frequency range up to 10 GHz.

[38] A. G. Veselov, S. L. Vysockiy, G. T. Kazakov, A. G. Sukharev, and Y. A. Filimonov, J. Commun. Technol. Electron. **39**, 102 (1994).

[39] V. E. Demidov, B. A. Kalinikos, S. Karmanenko, A. Semenov, and P. Edenhofer, IEEE Trans. Microwave Theory Tech. **51**, 2090 (2003).

[40] Y. K. Fetisov and G. Srinivasan, Appl. Phys. Lett. **87**, 103502 (2005).

[41] OMEGA Engineering, Inc. Mechanically polished YIG is bonded to the PZT using OMEGA's TT300 cement heat-cured, two-part epoxy adhesive based on ethyl 2-cyanoacrylate $C_6H_7NO_2$ for strain measurement.

[42] R. W. Damon and J. Eschbach, J. Phys. Chem. Solids **19**, 308 (1961).

[43] D. D. Stancil and A. Prabhakar, *Spin Waves: Theory and Applications* (Springer, New York, 2009).

[44] P. P. Silvester and R. L. Ferrari, *Finite Elements for Electrical Engineers* (Cambridge University Press, Cambridge, England, 1996).

[45] Calculated using COMSOL Multiphysics software from COMSOL, Inc.

[46] A. Sadovnikov and A. G. Rozhnev, Appl. Nonlinear Dyn. **20**, 143 (2012).

[47] A. V. Sadovnikov, A. A. Grachev, E. N. Beginin, S. E. Sheshukova, Y. P. Sharaevskii, A. A. Serdobintsev, D. Mitin, and S. A. Nikitov, IEEE Trans. Magn. **53**, 2801604 (2017).

[48] Calculated using the MATLAB with COMSOL Multiphysics server, The MathWorks, Inc.

[49] A. Vansteenkiste, J. Leliaert, M. Dvornik, M. Helsen, F. Garcia-Sanchez, and B. Van Waeyenberge, AIP Adv. **4**, 107133 (2014).

[50] M. Koshiba, K. Hayata, and M. Suzuki, J. Lightwave Technol. **4**, 121 (1986).

[51] G. Srinivasan, S. Priya, and N. Sun, *Composite Magnetoelectrics Materials, Structures, and Applications* (Woodhead, New York, 2015).

[52] The scale factor for the geometry transformation is 80 to improve the visualization of the calculated data.

[53] H. Sasaki and N. Mikoshiba, Electron. Lett. **15**, 172 (1979).

[54] L. R. Adkins and H. L. Glass, J. Appl. Phys. **53**, 8928 (1982).

[55] P. Grünberg, J. Appl. Phys. **51**, 4338 (1980).

[56] A. Weierholt, A. Mickelson, and S. Neegard, IEEE J. Quantum Electron. **23**, 1689 (1987).

[57] S. O. Demokritov, B. Hillebrands, and A. N. Slavin, Phys. Rep. **348**, 441 (2001).

[58] S. O. Demokritov and V. E. Demidov, IEEE Trans. Magn. **44**, 6 (2008).

[59] V. E. Demidov and S. O. Demokritov, IEEE Trans. Magn. **51**, 0800215 (2015).

[60] A. Vansteenkiste and B. Van de Wiele, J. Magn. Magn. Mater. **323**, 2585 (2011).

[61] S. Rushin and E. Marom, J. Opt. Soc. Am. A **1**, 1120 (1984).

[62] R. J. McCosker and G. E. Town, Sens. Actuators B **150**, 417 (2010).

[63] V. E. Demidov, S. Urazhdin, A. Zholud, A. V. Sadovnikov, and S. O. Demokritov, Appl. Phys. Lett. **106**, 022403 (2015).